


Interlayer and excited-state exciton transitions in bulk $2H$ -MoS₂

Vishwas Jindal,¹ Dipankar Jana,¹ Thorsten Deilmann^{2,*} and Sandip Ghosh^{1,†}

¹*Department of Condensed Matter Physics and Materials Science, Tata Institute of Fundamental Research, Homi Bhabha Road, Mumbai 400005, India*

²*Institut für Festkörperteorie, Westfälische Wilhelms-Universität Münster, 48149 Münster, Germany*

 (Received 8 July 2020; revised 27 August 2020; accepted 4 December 2020; published 18 December 2020)

Photoreflectance (PR) spectrum of bulk $2H$ -MoS₂ at energies around its direct band gap is shown to have at least three distinct spectral features over a certain temperature range, although only two are seen in absorption and reflectance spectra. These observations are compared with results from many-body perturbation theory band structure calculations that include exciton formation through the Bethe-Salpeter equation. Apart from the ground state A ($n = 1$) exciton transition around 1.92 eV at 25 K, the next spectral feature around 1.96 eV, whose origin has been much debated, is identified here with a transition I with strong interlayer contributions. Its greater sensitivity to electric fields is established through electroreflectance measurements. The third one around 1.99 eV, which is prominent only in PR, is shown to arise from the first excited state A ($n = 2$) exciton transition. We discuss the previously unexplained observation as to why the A ($n = 2$) feature dominates the PR spectrum at high temperatures. The A exciton is shown to have a quasi-two-dimensional (2D) nature with binding energy of 77 ± 3 meV under a 2D hydrogenic exciton model.

DOI: [10.1103/PhysRevB.102.235204](https://doi.org/10.1103/PhysRevB.102.235204)

I. INTRODUCTION

The continuing interest in transition metal dichalcogenide (TMDC) semiconductors like MoS₂ is driven by the discovery in the past decade of novel properties of their stable two-dimensional (2D) mono/few layer forms. These properties include layer number dependent indirect-to-direct band-gap transition, large exciton and trion binding energies, spin-valley coupling, valley coherence, etc., which hold promise for novel device applications [1–3]. This in turn has led to a reassessment of their electronic band structure (EBS) even in bulk form, while trying to understand how it transforms in mono/few layers. For instance, photoemission spectroscopy studies have shown that even in bulk there is spin-layer coupling whereby the valence band spins in adjacent Mo-S layers along the c axis are coupled in an anti-parallel manner [4]. In bulk $2H$ -MoS₂, which is the most naturally abundant polymorph, the Mo-S layers are held together by weak van der Waals forces along the c axis. It is an indirect band-gap semiconductor, its direct band gap arises at the K point of the Brillouin zone (BZ). Since the direct band gap in monolayer MoS₂ also arises at the K point, it is important to understand the EBS of bulk MoS₂ around this point. Also since exciton binding energy E_b in mono/few layer TMDCs can be very large, reaching several hundred meV, excitons play a crucial role in determining optical, transport, and consequently device properties, and have been studied extensively [5,6]. It is therefore essential to understand properties of excitons in bulk MoS₂ as a starting point.

At low temperatures around the direct band gap of bulk $2H$ -MoS₂, one observes two strong resonant features at $\simeq 1.92$

and $\simeq 2.12$ eV in optical absorption (Abs) and reflectance (R) spectra. They arise from exciton transitions involving two conduction bands (split by a few meV) and two spin-orbit split valence bands at the K point of the BZ and are referred to as the ground state A ($n = 1$) and B ($n = 1$) excitons [7–9]. About 35 meV above A ($n = 1$), one finds another weak resonant feature in these spectra, which we shall call $X1$. Early modulation spectroscopy (MS) measurements such as electroreflectance/absorption spectroscopy showed more features, sometimes a prominent one at energies just above $X1$, which we shall call $X2$ [10–13]. In these early studies, two issues that often came up were the origins of the features $X1$ and $X2$ and the reason why $X2$ was at times a stronger feature than A ($n = 1$) in a MS measurement. $X2$ was usually labeled as an “antiresonance” feature [7,13] and its relatively larger strength in MS data was never satisfactorily explained. There have been more reports related to $X1$.

The early literature identified $X1$ with the first excited state A ($n = 2$) of the A exciton [7–13]. Then using energies of A ($n = 1$) and A ($n = 2$) these reports obtained E_b for A exciton within the effective-mass hydrogenic model to be in the range 50–58 meV [7,13]. However even in the early days the assignment of $X1$ as A ($n = 2$) had problems. Reports which claimed to have seen even higher excited states of A exciton found that the extrapolated ground state transition energy based on the hydrogenic exciton model was off by 70–90 meV from the measured value [8,9]. This was explained as some ground state anomaly. Also magnetic circular dichroism studies showed that the Landé g -factor for $X1$ had an opposite sign and much larger magnitude than that for A ($n = 1$), which is not expected for an excited state of the same exciton [14]. More recently it was suggested that this weaker $X1$ feature in Abs and R spectrum could originate from an altogether different exciton transition at the H point of the BZ of bulk

*thorsten.deilmann@wwu.de

†sangho10@tifr.res.in

$2H$ -MoS₂ [15,16]. In the latest studies on bilayer $2H$ -MoS₂, a spectral feature seen at energies in between A and B exciton features has been identified with a new type of exciton, the “interlayer” exciton [17].

There is also the question regarding the dimensionality of the excitons. Because of the weak bond between adjacent Mo-S layers, bulk MoS₂ had been studied in the 1970s as a 2D material candidate with experimental evidence from infrared magneto-optical [18] and tunneling measurements [19]. However the above mentioned early optical studies [7–9,13] considered a 3D exciton model to explain the spectral features in $2H$ -MoS₂ and to determine E_b . Recent photoemission studies indicate that electronic states in bulk MoS₂ have a quasi 2D nature [20]. Also newer theoretical studies suggest that in bulk $2H$ -MoS₂ the exciton ground state is predominantly confined in a single Mo-S layer giving it a 2D character [21].

Here we report a combined Abs, R, photoreflectance (PR), and electroreflectance (ER) spectroscopy study of bulk $2H$ -MoS₂ at energies around its direct band gap. One finds exciton related spectral features, which show up prominently only in PR, with unusual temperature dependent properties. We try to understand our results with the help of density functional theory (DFT) based EBS calculations, as well as many-body perturbation theory in the GW approximation which take into account Coulomb interactions through the Bethe-Salpeter equation (BSE) yielding the theoretical exciton Abs spectrum. The study attempts to unravel the above questions related to the origins of the $X1$ and $X2$ features, including the latter’s unusual properties, with consequences for the dimensionality and binding energy of the A exciton.

II. EXPERIMENTAL DETAILS

The samples were small exfoliated flakes of $2H$ -MoS₂ of geological origin and were put onto double side polished sapphire substrates. A thin flake (27 nm thick, ~ 43 monolayers) was chosen for Abs measurements [22]. R and PR measurements were done on flakes several tens of microns thick. The samples were cooled using a continuous flow He cryostat with optical access. The probe beam was obtained by dispersing light from a 75 W Xenon lamp using a 0.5 m focal length monochromator. A microscope arrangement using 20X/50X long working distance objectives, was coupled to the monochromator output and helped achieve a measurement spatial resolution of $\sim 15 \times 30 \mu\text{m}^2$ for PR and $\sim 6 \times 12 \mu\text{m}^2$ for Abs, R, and ER. A camera plus illumination source was also included in the above setup to enable identification of a clean area on the sample, check the focusing of the probe and pump beam along with their spatial coincidence. For PR measurements, the pump beam was a 532-nm frequency doubled Nd-YAG laser. For ER spectroscopy, Al contacts were coated on a thick sample by thermal evaporation. During measurements the probe beam was positioned very close to a contact [22]. A small alternating voltage (0.5 V_{pp}, 175 Hz) was applied which modulated the built-in electric field near the contact to generate the ER signal. This arrangement, when compared to a non-microscope based conventional PR/ER setup, helped in getting data from a uniform clean region of the sample and improved the data quality. A photomultiplier

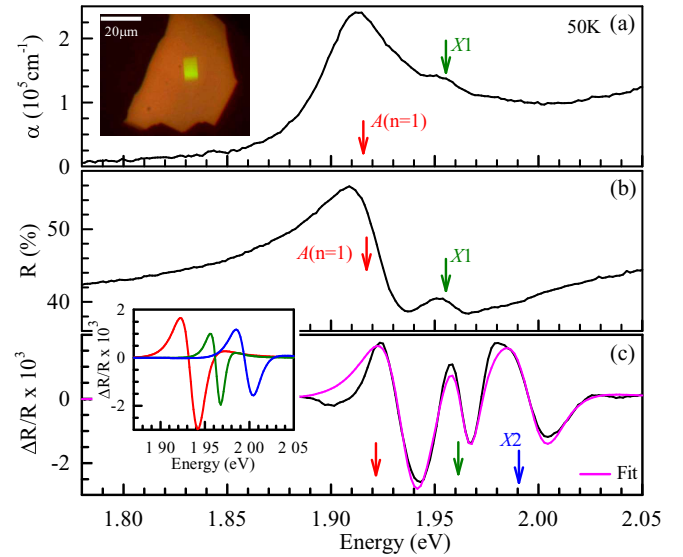


FIG. 1. (a) Absorption (Abs), (b) reflectance, and (c) photoreflectance (PR) spectrum of bulk $2H$ -MoS₂ around its direct band gap at 50 K. The inset in (a) is an optical image of the flake on sapphire substrate used for Abs measurement. It also shows the focused monochromatized probe beam spot. In (a) and (b), only two transitions A ($n = 1$) and $X1$, are clearly seen. The line-shape fitting in (c) using Aspnes’ line-shape function required a third transition $X2$. The inset in (c) shows the three individual fitted PR line-shapes. We later identify $X1$ with interlayer I and $X2$ with excited state A ($n = 2$) exciton transitions.

tube and Lock-in amplifier combination was used for phase sensitive signal detection.

III. EXPERIMENTAL RESULTS

Figure 1(a) shows the measured Abs spectrum of bulk $2H$ -MoS₂ at 50 K. Figure 1(b) shows the R spectrum. In both spectra, one observes a dominant feature attributed to the ground state A ($n = 1$) exciton transition and on its high energy side a weaker feature $X1$. The B ($n = 1$) exciton related feature of bulk $2H$ -MoS₂ is seen at higher energies [22] and will not be discussed further here. As mentioned before, $X1$ had originally been identified as the A ($n = 2$) excited state transition and thereafter as possibly a new exciton transition at the H point of the BZ of bulk $2H$ -MoS₂. Figure 1(c) shows the measured PR spectrum of the sample at 50 K, which clearly seems to have one more feature. The usual approach for analyzing a PR spectrum involves fitting Aspnes’ differential functional form line-shape function [23]. We needed at least three transitions to fit the measured spectrum shown in Fig. 1(c). The inset in Fig. 1(c) shows the three individual fitted line-shapes. Thus apart from the A ($n = 1$) and $X1$ features, the PR spectrum has a third feature labeled $X2$, which is quite prominent at 50 K, although it is seemingly absent in the R and Abs spectra. Henceforth we will identify $X1$ with an “interlayer” exciton I and $X2$ with the excited state A ($n = 2$) exciton, which we shall justify subsequently. Figures 2(a) and 2(b) show the measured R and PR spectrum of bulk $2H$ -MoS₂ at different temperatures in the range 25 to 297 K. It is evident that this third transition A ($n = 2$) is actually the dominant PR

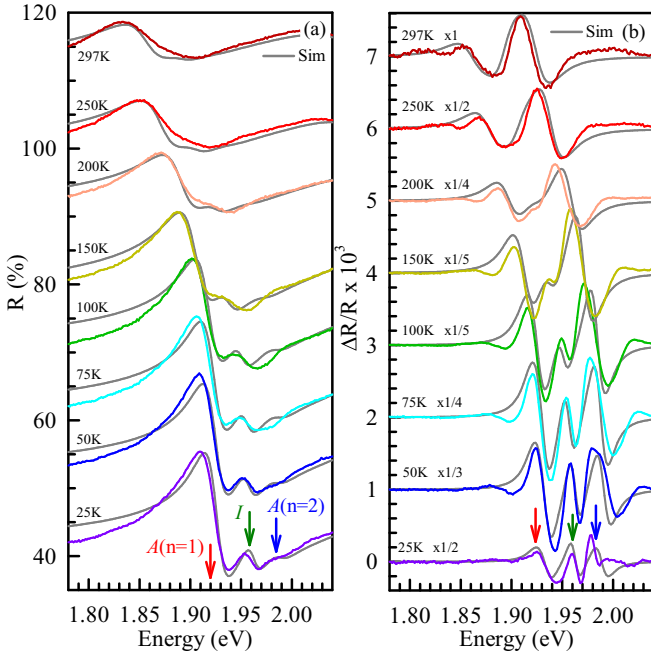


FIG. 2. Measured and simulated (a) R and (b) PR spectra of bulk $2H$ -MoS₂ around its direct band gap at various temperatures. For clarity, R and scaled PR plots are vertically displaced in steps of 10% and 1×10^{-3} , respectively. Line-shape simulations starting from Eq. (1) consider three transitions identified as $A(n=1)$, interlayer I and excited state $A(n=2)$ exciton transitions.

feature around room temperature, although in R the $A(n=1)$ transition dominates throughout.

In general for an exciton transition, the PR signal magnitude depends on the exciton oscillator strength, as well as the strength of the modulation. Aspnes' line-shape fitting alone cannot easily distinguish between these two contributions and throw light on the modulation mechanism. Such information however can give clues about the origins of the PR features and to resolve it we have adopted the following approach. We simulate the PR spectrum from first principles and compare it with the measured spectrum to extract the modulation mechanism and its strength. We begin with the Lorentz oscillator model to describe the exciton contribution to the dielectric function $\varepsilon(E)$ as

$$\varepsilon(E) = \varepsilon_b + \sum_j \frac{C_j}{E_{0j}^2 - E^2 - i\Gamma_j E}, \quad (1)$$

where E is the photon energy while E_{0j} , Γ_j and C_j are the transition energy, broadening and oscillator strength parameter for the j^{th} exciton transition, respectively. ε_b is the background dielectric constant that is relatively weakly dependent on photon energy. In our simulations we find an average value of 22.1 at photon energies around 1.92 eV. In general the exciton PR spectrum arises because of one or more of the following changes $E_{0j} \rightarrow E_{0j} \pm \Delta E_{0j}$, $\Gamma_j \rightarrow \Gamma_j \pm \Delta \Gamma_j$ and $C_j \rightarrow C_j \pm \Delta C_j$, due to the laser modulation. Also for exciton transitions, the PR spectrum is known to have a first derivative nature [24]. Equation (1) leads us to the real and imaginary parts of the refractive indices with which we first simulate the R spectrum assuming normal incidence and

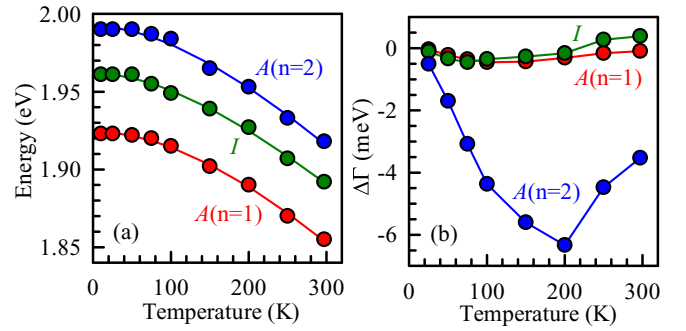


FIG. 3. (a) Temperature dependence of the three exciton transition energies estimated from simulations of R and PR spectrum. The lines are fits using the Varshini equation. (b) Temperature dependence of $\Delta\Gamma$ parameter for the three simulated PR features corresponding to $A(n=1)$, I , and $A(n=2)$ exciton transitions.

values of E_{0j} , Γ_j and C_j that best reproduce the measured R spectrum. We then calculate a modified R' spectrum by introducing changes ΔE_{0j} , $\Delta \Gamma_j$, ΔC_j . The PR spectrum is then obtained as $\Delta R/R = (R' - R)/R$. PR spectral line-shapes depend on the modulation mechanism, whether ΔE_{0j} , $\Delta \Gamma_j$, ΔC_j or their combination and the sign of the change [22]. Figures 2(a) and 2(b) also show the simulated R and PR spectrum of bulk $2H$ -MoS₂ at various temperatures based on the above formalism, considering three transitions ($j = 1, 2, 3$). In initially choosing the C value for $A(n=2)$, we were guided by the theoretical results, which are discussed later. It is evident that the main spectral features of both R and PR spectra are fairly well reproduced in the simulations. We found that in the simulations only a decrease $-\Delta \Gamma_j$, when the pump laser is on, was sufficient to reproduce the measured spectra at temperatures above 25 K.

Figure 3(a) shows the temperature dependence of the three estimated transition energies E_{0j} . There is small difference up to $\simeq 6$ meV between E_{0j} values used in the simulation that best match the R and PR spectrum, which likely arises from our model's limitations. The temperature dependence of E_{0j} follows the expected behavior arising from the decrease in the band gap of a semiconductor with increase in temperature and are well fit by the phenomenological Varshini equation $E(T) = E(0) + aT^2/[b + T]$ with $E(0) = 1.924$ eV as the transition energy for temperature tending to 0 K, $a = 7.6 \times 10^{-4}$ eV/K and $b = 657$ K as best fit parameters for the $A(n=1)$ exciton. For comparison with b parameter, the energy equivalent temperature of the dominant LO phonons E_{2g}^1 and A_{1g} in bulk $2H$ -MoS₂ are 591 and 560 K, respectively. Our primary concern is $E(0)$, which for $A(n=1)$ exciton is similar to previous reports [7–9]. $E(0)$ for I and $A(n=2)$ is higher than that of $A(n=1)$ by 35 and 68 meV, respectively. The dependence of the strength of $\Delta \Gamma_j$ modulation, shown in Fig. 3(b) is more interesting. While $\Delta \Gamma_j$ remains relatively small for $A(n=1)$ and I transitions, its magnitude for $A(n=2)$ increases rapidly with increase in temperature, reaching a peak value which is an order of magnitude larger than that for $A(n=1)$ and I . The relatively large strength of the $A(n=2)$ feature in PR at high temperatures, while hardly showing up in R, is essentially due to this large modulation strength. To

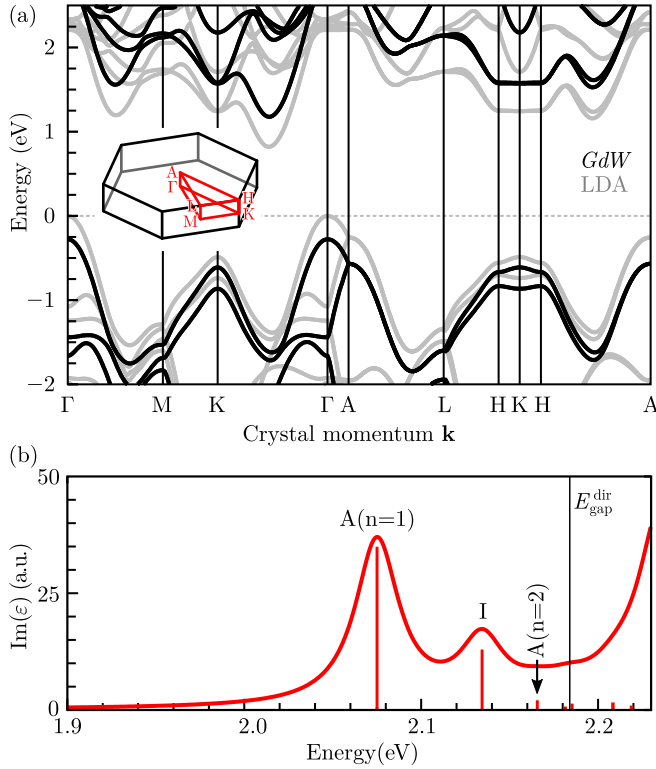


FIG. 4. (a) Electronic band structure of bulk $2H$ - MoS_2 with (black lines, GdW approximation) and without (gray lines, LDA) many body effects. The minimal direct gap is located at the K point. The schematic inset shows the first Brillouin zone. (b) Theoretical absorption spectrum of bulk $2H$ - MoS_2 including excitons by employing the BSE. The relative oscillator strengths are indicated by thick vertical lines.

understand these results we took the help of theoretical EBS calculations which is described next.

IV. ELECTRONIC BAND STRUCTURE CALCULATION RESULTS

Figure 4(a) shows the calculated EBS of bulk $2H$ - MoS_2 . The gray lines correspond to results from DFT in the local density approximation (LDA), while the black lines include many-body effects employing the GdW approximation [25]. Further numerical details can be found in Refs. [26–28]. The indirect band gap of bulk MoS_2 is found between Γ and about half of K - Γ with a magnitude of 1.45 eV (0.82 eV in DFT). The direct gap at K is significantly larger. Our calculations show that many-body effects increase the DFT gap from 1.73 to 2.18 eV. Note that for the top valence band, the energy–crystal momentum dispersion along H - K and H - L/A directions have opposite curvature. It indicates a saddle point like structure with no local maximum at the H point.

Figure 4(b) shows the calculated Abs spectrum of bulk $2H$ - MoS_2 employing the BSE [29]. Below the direct gap three transitions with significant oscillator strength can be identified. The lowest energy transition with the strongest absorption is identified as $A(n=1)$. At energies above $A(n=1)$, we find another transition labeled I and thereafter another much weaker one labeled $A(n=2)$. However after

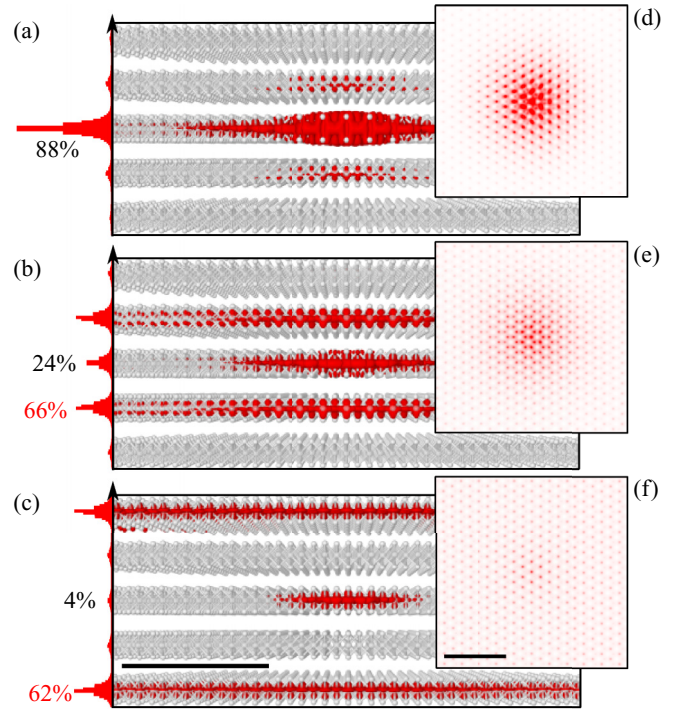


FIG. 5. x - z projection of the electron probability distribution $|\Psi|^2$ presented on a background of Mo-S crystal planes (gray) in bulk $2H$ - MoS_2 and its integrated projection along c axis (arrow) $\parallel z$ for (a) $A(n=1)$, (b) I , and (c) $A(n=2)$ excitons with $l=0$. Projection of $|\Psi|^2$ on to the x - y plane for (d) $A(n=1)$, (e) I , and (f) $A(n=2)$ excitons with $l=0$. The fixed hole is located in the center of each image. The black scale bars mark a length of 20 Å.

including a 40-meV Lorentzian broadening the $A(n=2)$ spectral feature is smeared out in the calculated Abs spectrum. This is consistent with the measured Abs spectrum in Fig. 1(a) where too we do not see a prominent third feature. These three have theoretical binding energies of about 110, 50, and 20 meV. All these transitions are associated with states at or very close to the $\pm K$ points of the BZ.

In Figs. 5(a) and 5(c), we have plotted the x - z projection of the electron probability distribution $|\Psi|^2$ (red) in the $A(n=1)$, I , and $A(n=2)$ states, respectively. Here for $A(n=2)$, the $2s$ state (angular momentum $l=0$) is shown, the $2p$ state ($l=1$) was found to be optically dark. In all plots the hole position is fixed in the center of the middle Mo-S layer. Also shown on the left side is the projection of $|\Psi|^2$ along the c axis. The numbers represent the integrated electron probability distribution in the central layer (black text), and the sum of the next or second next layers (red text). We find that the electron probability distribution in the $A(n=1)$ state is concentrated in the same layer as the hole, in agreement with earlier reports [21]. For the I state, the electron probability distribution is more in the adjacent layers, which are rotated by 180° with respect to the neighboring layer, with the inter-layer spacing/Mo-Mo distance along c axis being ~ 6.14 Å. For $A(n=2)$ the electron probability distribution is mostly localized in the second next layers away from the hole.

Figures 5(d)–5(f) show the projections of $|\Psi|^2$ on to the x - y plane for the $A(n=1)$, I , and $A(n=2)$ exciton states,

respectively. Due to the reduced Coulomb interaction in the I state, the overall spread of the exciton in this state is enhanced in the x - y plane with respect to A ($n = 1$). For the A ($n = 2$) exciton, within the range of our calculation which extends up to ~ 30 Å from the origin in the x - y plane, $|\Psi|^2$ is widely extended and does not decay to zero. A more precise determination requires more than the employed $21 \times 21 \times 6$ k points.

Finally, we underline that in our calculations we observe no exciton solely located close to the H point. Although the magnitude of the energy gap at the H point suggests the possibility [15,16] that the $X1$ transition is associated with an exciton there, the EBS in Fig. 4(a) around the H point, which was discussed earlier, prohibits such exciton states.

V. DISCUSSION

While the absolute value of the theoretical transition energies is not expected to be more accurate than 0.1–0.2 eV, the relative positions and intensities of spectral features are much more reliable [29]. Comparing the relative positions and strengths of $X1$ and $X2$ feature in Figs. 1(a) and 1(b) with the theoretical results in Fig. 4(b) we identified $X1$ with an interlayer exciton I and $X2$ with the A ($n = 2$) exciton transition. We will further justify these assignments. Optical transition involving A ($n = 1$) state has predominant oscillator strength as seen from Fig. 4(b), which is in agreement with measured R and Abs data. We saw in Fig. 5(a) that the electron probability distribution in the A ($n = 1$) state, is strongly anisotropically confined to a single Mo-S plane giving it a 2D character. The oscillator strength of A ($n = 2$), as obtained from the simulations in Fig. 2, is lower than that of A ($n = 1$) by a factor $1/18$ (~ 0.06), which is close to $1/27$ (~ 0.04) expected in an exact 2D hydrogenic exciton model where oscillator strength goes as $1/[n - 1/2]^3$ [30]. For the I transition, the oscillator strength was lower by a factor of $1/8$ (0.125) and so does not match the expectation for A ($n = 2$) in the 2D hydrogenic exciton model.

In the 2D hydrogenic exciton model, the energy difference $E_{n=2} - E_{n=1} = 8/9 E_b$, where E_b is the exciton binding energy. If we analyze the A ($n = 1$) and A ($n = 2$) transition energy spacings using this model with $X2$ identified as A ($n = 2$), we obtain $E_b = 77 \pm 3$ meV. Since in the 2D model $E_b = 4R_y^*$, we get an effective Rydberg constant $R_y^* \sim 19$ meV. One can also arrive at R_y^* from material parameters since $R_y^* = 13.6 \mu/\varepsilon_r^2$ eV, where ε_r is the effective dielectric constant and μ is the reduced effective mass of the electron-hole pair. In an anisotropic material like $2H$ -MoS₂, ε_r is dependent on the polarization of light relative to the \mathbf{c} axis and is given by $\varepsilon_r = \sqrt{\varepsilon_{r\parallel\mathbf{c}} \varepsilon_{r\perp\mathbf{c}}}$. [31] With $\varepsilon_{r\parallel\mathbf{c}} \sim 8$ from averaged theoretical predictions [21,31], $\varepsilon_{r\perp\mathbf{c}} = \varepsilon_b \sim 22.1$ from our reflectance simulations, electron and hole effective masses [32] being $m_e^* = 0.46m_0$ and $m_h^* = 0.45m_0$ respectively, we get $R_y^* \sim 18$ meV from material parameters. This is in very good agreement with the above estimate based on A ($n = 1$) and A ($n = 2$) energy spacing, again supporting the assignment of $X2$ as A ($n = 2$) and the 2D hydrogenic model. In a homogeneous 3D model, we would have $E_{n=2} - E_{n=1} = 3/4 R_y^*$ resulting in a $R_y^* \sim 91$ meV which is significantly larger than what we obtained based on material parameters. Similarly if

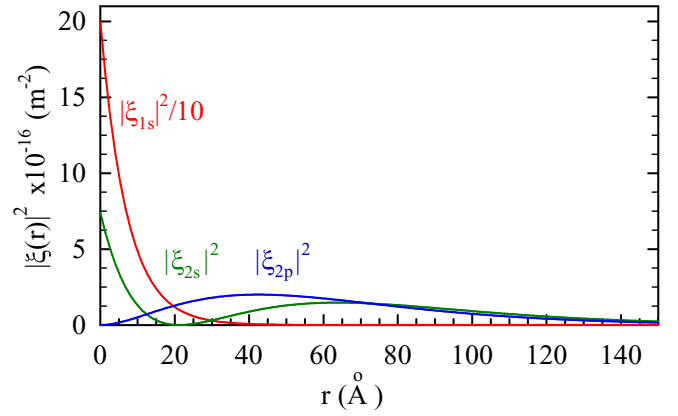


FIG. 6. Radial electron probability distribution for the $n = 1$ and 2 ($l = 0 : 2s$ and $1 : 2p$) states, in a 2D hydrogenic exciton model with effective Bohr radius 28 Å.

we had wrongly identified $X1$ as A ($n = 2$) in a 2D model, we would get $R_y^* \sim 9.8$ meV, again very different from the value obtained from material parameters. Note that our value of E_b here is much larger than the earlier estimates [7,13] which were in the range 50–58 meV based on wrongly identifying $X1$ feature with the A ($n = 2$) transition, but is closer to the estimate of 84 ± 5 meV reported more recently [33]. Figure 6 shows the in-plane radial electron probability distribution $|\xi(r)|^2$ as a function distance r from the center of mass origin in a 2D hydrogenic exciton model, for $n = 1$ and $n = 2$ states [22]. The effective Bohr radius here was calculated using $a_0^* = e^2/[8\pi\varepsilon_0\varepsilon_r R_y^*] \sim 28$ Å. In Fig. 6, we see that the radial electron probability distribution in the $n = 1$ state peaks at the origin and falls off on a scale very similar to $|\Psi|^2$ for A ($n = 1$) in Figs. 5(a) and 5(d), which is concentrated in the x - y plane, again justifying a 2D hydrogenic model. However in the A ($n = 2$) with $l = 0$ state in Fig. 5(c), the electron probability distribution is more spread out along the \mathbf{c} axis $\parallel \hat{\mathbf{z}}$. Although one cannot therefore expect an exact match with the 2D hydrogenic model, we do find that $|\Psi|^2$ for our assigned A ($n = 2$) state with $l = 0$, in the central Mo-S layer containing the hole, also peaks at the origin like the $2s$ state in the 2D hydrogenic model in Fig. 6. We could not extend the BSE calculations to a larger lattice, to observe any broader peaking of $|\Psi|^2$ in a A ($n = 2$) state further away from origin as in $2s$ Fig. 6, due to computational limitations.

Figures 5(b) and 5(e) show that for our assigned I state, the projection of $|\Psi|^2$ in the x - y plane is concentrated around the hole and in adjacent Mo-S layers. There is no analog for such an excited state at this energy in a 2D hydrogenic model. Existence of such a unique exciton state was first reported in few layer TMDCs only recently [17,26,27,34] and were labeled “interlayer excitons” because the electron probability distribution along the \mathbf{c} axis is highest in layers just adjacent to the Mo-S layer where the hole is. Note that this is different from an interlayer exciton in a heterostructure where the electron and hole reside on two sides of a junction of two dissimilar materials. Here it is the same material throughout. We also note that the different spin structure of the bands in case of 3R type stacking results in the absence of an I exciton

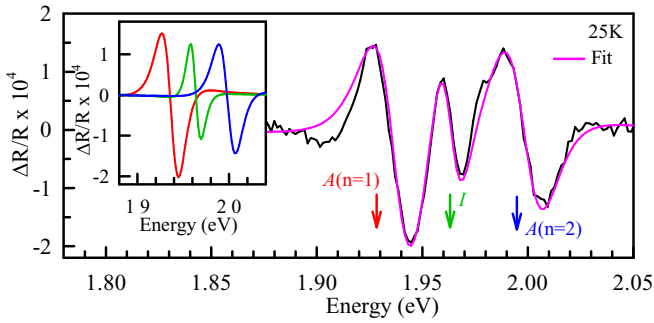


FIG. 7. Electroreflectance (ER) spectrum of bulk $2H$ - MoS_2 around its direct band gap at 25 K showing features originating from $A(n=1)$, I and $A(n=2)$ exciton transitions, fitted with Aspnes' line-shape function. Inset shows the fitted individual line-shapes.

in $3R$ - MoS_2 . This has been observed in bi-layer MoS_2 with $3R$ type stacking [35] and in bulk $3R$ - MoS_2 [36].

Very recently similar interlayer excitons in trilayer $2H$ - MoS_2 were shown to exhibit weak Stark splitting at electric fields of ~ 1 MV/cm [37]. It is difficult to generate such high fields in bulk samples in order to observe Stark splitting. Note that the spread of the electron cloud in the Mo-S layer adjacent to the one with the hole results in reduced Coulomb attraction. In addition, the Mo-S layers along the c axis are only weakly coupled through van der Waal's forces. Consequently one expects the I exciton to show greater sensitivity to electric fields in general. We have tested this as follows. Figure 7 depicts the ER spectrum of bulk $2H$ - MoS_2 at 25 K which again shows features originating from our designated $A(n=1)$, I and $A(n=2)$ exciton transitions. Here the built-in electric field close to the electrode, which has vertical ($\parallel c$ axis) and lateral components is being modulated [22]. Both components should affect the I exciton more than $A(n=1)$. The strength of an exciton feature in an ER spectrum depends both on the oscillator strength and the modulation strength, the latter being the measure of its sensitivity to electric fields. The broadening independent strength of an exciton feature in a modulated reflectance spectrum can be quantified through the product $a\gamma^2$, where a and γ are modified amplitude and broadening parameters in Aspnes' line-shape function.[23] The ratio $a\gamma^2$ for I to that for $A(n=1)$, obtained from fitting Aspnes' line-shape function to the ER spectrum in Fig. 7, is found to be $1/4$. The ratio of oscillator strengths of I to $A(n=1)$ obtained from fitting the R spectrum was already mentioned to be $1/8$. This suggests that the I feature relative to $A(n=1)$ is stronger in the ER spectrum in Fig. 7 than in the R spectrum at 25 K in Fig. 2(a), which is also evident from a visual inspection. Thus the electric field induced modulation for our designated I exciton transition is much larger compared to that for $A(n=1)$ exciton, thereby supporting our interpretation of its origins.

Although we have considered a 2D hydrogenic exciton model, we noted earlier that in the $A(n=2)$ state in Fig. 5(c) the electron probability distribution does spread along the c axis $\parallel \hat{z}$, being mostly in the third layer which is about 12.3 \AA from the hole. However this spread along \hat{z} is much smaller than what is expected in a homogeneous 3D model [22]. This spread of the $A(n=2)$ state along the c axis, which relative to

$A(n=1)$ is fairly large, can have an important consequence. Since there exists only a weak van der Waals force holding the crystal together along the c axis, a perturbation in general is likely to affect the $A(n=2)$ state more. This phenomenon has also been seen in case of bulk WS_2 [28]. This can explain the much higher sensitivity of $A(n=2)$ to perturbation in a modulation spectroscopy measurement like PR, as evident from its relatively much larger $\Delta\Gamma$ modulation strength in Fig. 3(b) at higher temperatures, thereby making $A(n=2)$ the dominant PR spectral feature at room temperature.

Next we discuss some aspects of the PR modulation mechanism. In a typical PR measurement on group IV, III-V, or II-VI semiconductors and their 2D heterostructure QWs, the absorbed pump laser beam generates electron-hole pairs that reduce the built-in electric field present at the surface/interfaces. For an excitonic transition, the change in electric field gives rise to either ΔE_{0j} , $\Delta\Gamma_j$, ΔC_j , or a combination of these, and thereby the PR signal. For instance, in GaAs QWs, ΔE_{0j} is usually the dominant mechanism arising from a shift in the QW energy levels, which determines the effective band gap, through electric field induced quantum confined Stark effect [24,30]. Note that E_{0j} is determined by two components, the effective band gap and E_b . To understand the present case first note that E_b here is very large, nearly 20 times larger than in GaAs (~ 4 meV). E_b is also very sensitive to the background dielectric environment since $E_b \propto R_y^* \propto 1/\epsilon_r^2$. In mono/few layer TMDCs it has been shown that local changes in Coulomb interaction due to fluctuations of the external dielectric environment result in exciton spectral broadening represented here by the parameter Γ [38]. This is in addition to the phonon induced contribution to Γ which increases with rise in temperature. Encapsulation with hexagonal boron nitride [39] can change the effective ϵ_r and fluctuations in it, the latter especially can dramatically reduce Γ . It is therefore possible that in the present case, at high temperature, the dominant effect is that of photogenerated carriers influencing the ϵ_r spread, giving rise to the observed predominantly $\Delta\Gamma_j$ modulation mechanism in PR. If ionized impurities are the source of ϵ_r spread and their neutralization by photogenerated carriers reduces the inhomogeneity, then it would result in $-\Delta\Gamma_j$ modulation. Starting from low temperature, an increase in impurity ionization with increase in temperature, as evident from temperature dependent carrier concentration measurements [40] on MoS_2 , possibly increases the ϵ_r spread. Consequently there is more ϵ_r spread that can be reduced by the pump generated carriers as temperature rises, giving rise to the trend of increasing $\Delta\Gamma_j$ modulation with increase in temperature. However, after 200 K, one finds that $|\Delta\Gamma|$ starts to decrease and for I it also seems to change sign thereafter. This might be related to the saturation of impurity ionization coupled with an increase in intrinsic carrier concentration, the latter diminishing the role of photo-generated carriers in suppressing the ϵ_r spread, or the relatively stronger phonon contribution to Γ at higher temperatures. This aspect needs to be studied further.

VI. CONCLUSION

In conclusion, our study suggests that the long debated feature in the Abs and R spectrum of bulk $2H$ - MoS_2 , which was

previously suggested to arise from the excited state A ($n = 2$) exciton transition or a new exciton transition at the H point of the BZ, instead originates from an inter-layer exciton transition at the K point of the BZ. The inter-layer exciton is unique to some bulk TMDCs like $2H$ -MoS₂ with crystal structure having layers coupled by van der Waals forces. The A ($n = 2$) transition related feature can however be seen prominently in a modulated reflectance measurement such as PR and ER. Its origins had not been understood earlier, although it dominates the PR spectrum at room temperature. This occurs because the relatively larger spread of electron probability distribution in the A ($n = 2$) state along the c axis, along which only weak van der Waals forces hold the crystal together, makes it much more sensitive to perturbations. The A exciton in bulk $2H$ -MoS₂ is shown to have a quasi 2D nature and the binding energy is estimated to be up to 50% larger than previously thought. The modulation mechanism in PR at high tempera-

ture was found to be dominated by a change in the spectral broadening parameter and the strength of the modulation varied with temperature, for which a provisional explanation was provided.

ACKNOWLEDGMENTS

The authors thank V. Sugunakar for help with instrumentation and A. Arora for very useful discussions. T.D. acknowledges financial support from German Research Foundation (DFG Project No. DE 2749/2-1) and the computing time granted by the John von Neumann Institute for Computing and provided on the supercomputer JUWELS of the Jülich Supercomputing Centre. S.G. acknowledges support of the Department of Atomic Energy, Government of India Project No. 12-R&D-TFR-5.10-0100.

-
- [1] A. V. Kolobov and J. Tominaga, *Two-Dimensional Transition-Metal Dichalcogenides* (Springer, Switzerland, 2016).
- [2] J. Pu and T. Takenobu, *Adv. Mater.* **30**, 1707627 (2018).
- [3] T. Mueller and E. Malic, *npj 2D Mater. Appl.* **2**, 29 (2018).
- [4] R. Suzuki, M. Sakano, Y. J. Zhang, R. Akashi, D. Morikawa, A. Harasawa, K. Yaji, K. Kuroda, K. Miyamoto, T. Okuda, K. Ishizaka, R. Arita, and Y. Iwasa, *Nat. Nanotech.* **9**, 611 (2014).
- [5] J. Xiao, M. Zhao, Y. Wang, and X. Zhang, *Nanophotonics* **6**, 1309 (2017).
- [6] G. Wang, A. Chernikov, M. M. Glazov, T. F. Heinz, X. Marie, T. Amand, and B. Urbaszek, *Rev. Mod. Phys.* **90**, 021001 (2018).
- [7] A. R. Beal, J. C. Knights, and W. Y. Liang, *J. Phys. C: Solid State Phys.* **5**, 3540 (1972).
- [8] E. Fortin and F. Raga, *Phys. Rev. B* **11**, 905 (1975).
- [9] M. R. Khan and G. J. Goldsmith, *Il Nuovo Cimento* **2**, 665 (1983).
- [10] J. Bordas and E. A. Davis, *Phys. Stat. Sol. B* **60**, 505 (1973).
- [11] H. Meinhold and G. Weiser, *Phys. Stat. Sol. B* **73**, 105 (1976).
- [12] R. Murray and B. L. Evans, *Phys. Stat. Sol. B* **92**, 551 (1979).
- [13] K. K. Tiong and T. S. Shou, *J. Phys.: Condens. Matter* **12**, 5043 (2000).
- [14] M. Tanaka, H. Fukutani, and G. Kuwabara, *J. Phys. Soc. Jpn.* **45**, 1899 (1978).
- [15] N. Saigal and S. Ghosh, *Appl. Phys. Lett.* **106**, 182103 (2015).
- [16] J. Kopaczek, M. P. Polak, P. Scharoch, K. Wu, B. Chen, S. Tongay, and R. Kudrawiec, *J. Appl. Phys.* **119**, 235705 (2016).
- [17] I. C. Gerber, E. Courtade, S. Shree, C. Robert, T. Taniguchi, K. Watanabe, A. Balocchi, P. Renucci, D. Lagarde, X. Marie, and B. Urbaszek, *Phys. Rev. B* **99**, 035443 (2019).
- [18] R. Kaplan, *Phys. Rev. B* **14**, 4647 (1976).
- [19] D. Sarid, T. D. Henson, N. R. Armstrong, and L. S. Bell, *Appl. Phys. Lett.* **52**, 2252 (1988).
- [20] M. Gehlmann, I. Aguilera, G. Bihlmayer, E. Młyńczak, M. Eschbach, S. Döring, P. Gospodarič, S. Cramm, B. Kardynał, L. Plucinski, S. Blügel, and C. M. Schneider, *Sci. Rep.* **6**, 26197 (2016).
- [21] A. Molina-Sanchez and L. Wirtz, *Phys. Rev. B* **84**, 155413 (2011).
- [22] See Supplemental Material at <http://link.aps.org/supplemental/10.1103/PhysRevB.102.235204> for sample details, Abs and R spectra at higher energies, temperature dependence of oscillator strength and broadening parameter, PR line shapes for different modulation mechanisms, ER measurement details and also 2D and 3D hydrogenic radial wave functions.
- [23] S. Ghosh and H. T. Grahn, *J. Appl. Phys.* **90**, 500 (2001).
- [24] W. M. Theis, G. D. Sanders, C. E. Leak, K. K. Bajaj, and H. Morkoç, *Phys. Rev. B* **37**, 3042 (1988).
- [25] M. Drüppel, T. Deilmann, J. Noky, P. Marauhn, P. Krüger, and M. Rohlfing, *Phys. Rev. B* **98**, 155433 (2018).
- [26] A. Arora, M. Drüppel, R. Schmidt, T. Deilmann, R. Schneider, M. R. Molas, P. Marauhn, M. Potemski, M. Rohlfing, and R. Bratschitsch, *Nat. Commun.* **8**, 639 (2017).
- [27] A. Arora, T. Deilmann, P. Marauhn, M. Drüppel, R. Schneider, M. R. Molas, D. Vaclavkova, S. M. de Vasconcellos, M. Rohlfing, M. Potemski, and R. Bratschitsch, *Naonscale* **10**, 15571 (2018).
- [28] V. Jindal, S. Bhuyan, T. Deilmann, and S. Ghosh, *Phys. Rev. B* **97**, 045211 (2018).
- [29] M. Rohlfing and S. G. Louie, *Phys. Rev. B* **62**, 4927 (2000).
- [30] A. Mukherjee and S. Ghosh, *J. Appl. Phys.* **115**, 123503 (2014).
- [31] T. Cheiwchanchamnangij and W. R. L. Lambrecht, *Phys. Rev. B* **85**, 205302 (2012).
- [32] H. Peelaers and C. G. Van de Walle, *Phys. Rev. B* **86**, 241401(R) (2012).
- [33] N. Saigal, V. Sugunakar, and S. Ghosh, *Appl. Phys. Lett.* **108**, 132105 (2016).
- [34] J. Horng, T. Stroucken, L. Zhang, E. Y. Paik, H. Deng, and S. W. Koch, *Phys. Rev. B* **97**, 241404(R) (2018).
- [35] I. Paradisanos, S. Shree, A. George, N. Leisgang, C. Robert, K. Watanabe, T. Taniguchi, R. J. Warburton, A. Turchanin, X. Marie, I. C. Gerber, and B. Urbaszek, *Nat. Commun.* **11**, 2391 (2020).
- [36] J. Suh, T. L. Tan, W. Zhao, J. Park, D. Y. Lin, T. E. Park, J. Kim, C. Jin, N. Saigal, S. Ghosh, Z. M. Wong, Y. Chen, F. Wang, W. Walukiewicz, G. Eda, and J. Wu, *Nat. Commun.* **9**, 199 (2018).
- [37] N. Leisgang, S. Shree, I. Paradisanos, L. Sponfeldner, C. Robert, D. Lagarde, A. Balocchi, K. Watanabe, T. Taniguchi,

- X. Marie, R. J. Warburton, I. C. Gerber, and B. Urbaszek, [Nat. Nanotechnol.](#) **15**, 901 (2020).
- [38] A. Raja, L. Waldecker, J. Zipfel, Y. Cho, S. Brem, J. D. Ziegler, M. Kulig, T. Taniguchi, K. Watanabe, E. Malic, T. F. Heinz, T. C. Berkelbach, and A. Chernikov, [Nat. Nanotechnol.](#) **14**, 832 (2019).
- [39] F. Cadiz, E. Courtade, C. Robert, G. Wang, Y. Shen, H. Cai, T. Taniguchi, K. Watanabe, H. Carrere, D. Lagarde, M. Manca, T. Amand, P. Renucci, S. Tongay, X. Marie, and B. Urbaszek, [Phys. Rev. X](#) **7**, 021026 (2017).
- [40] S. Y. Wang, T. S. Ko, C. C. Huang, D. Y. Lin, and Y. S. Huang, [Jpn. J. Appl. Phys.](#) **53**, 04EH07 (2014).